JGR Solid Earth

RESEARCH ARTICLE
10.1029/2019JB017381

Special Section:
Physical Properties of Rocks, Friction and Fracturing: the Walsh Volume

Dynamics of Microscale Precursors During Brittle Compressive Failure in Carrara Marble

Neelima Kandula[1], Benoît Cordonnier[1,2], Elodie Boller[2], Jérôme Weiss[3], Dag Kristian Dysthe[1], and François Renard[1,3]

[1]The Njord Centre, PGP, Departments of Geosciences and Physics, University of Oslo, Oslo, Norway, [2]The European Synchrotron, ESRF, Grenoble, France, [3]University Grenoble Alpes, University Savoie Mont Blanc, CNRS, IRD, IFSTTAR, ISTerre, Grenoble, France

Key Points:
- Microfracture dynamics explains complex physical processes guiding the macroscopic failure in Carrara marble
- Statistical parameters measuring microfracture volume, growth, and spatial organization showed power law scaling with applied stress
- Evolution of several microstructural parameters is in agreement with models that establish compressive failure as a critical phase transition

Supporting Information:
- Supporting Information S1
- Movie S1
- Movie S2
- Movie S3
- Movie S4

Correspondence to:
N. Kandula,
neelima.kandula@geo.uio.no

Citation:
Kandula, N., Cordonnier, B., Boller, E., Weiss, J., Dysthe, D. K., & Renard, F. (2019). Dynamics of microscale precursors during brittle compressive failure in Carrara marble. *Journal of Geophysical Research: Solid Earth*, *124*, 6121–6139. https://doi.org/10.1029/2019JB017381

Received 17 JAN 2019
Accepted 30 MAY 2019
Accepted article online 6 JUN 2019
Published online 26 JUN 2019

©2019. The Authors.
This is an open access article under the terms of the Creative Commons Attribution-NonCommercial-NoDerivs License, which permits use and distribution in any medium, provided the original work is properly cited, the use is non-commercial and no modifications or adaptations are made.

Abstract Microscale heterogeneities influence failure mechanisms in the crust. To track the microstructural changes in rock samples when loaded until failure, we employed a novel experimental technique that couples dynamic X-ray microtomography imaging with a triaxial deformation apparatus. We studied the brittle failure of Carrara marble under triaxial compression. Dynamic tomographic data revealed the spatial organization of microfractures and damage increments characterizing the precursory activity toward catastrophic failure. We quantified the emergence of scaling relationships between microstructural parameters, including total damage volume, incremental damage volume, the largest connected microfracture, and the applied differential stress. The total volume of microfractures accumulated from the beginning of the experiment as well as the incremental damage showed power law increase. The growth of the largest connected microfracture was related to differential stress as a power law with divergence at failure. The microfracture volume increments were distributed according to a power law with an upper cutoff that itself spanned the entire volume toward failure. These characteristic features of brittle failure in Carrara marble under compression are in agreement with theoretical models that consider failure as a critical phase transition. We also observed that, very close to failure, several power law relationships broke down, which we interpret to be related to the coalescence of the largest microfractures in a finite size volume. Scaling laws and associated exponents computed from our data are compared with predictions made from theoretical and numerical models. Our results show that precursors of macroscopic brittle failure in Carrara marble follow predictable trends.

1. Introduction

Disorder and long-range stress interactions drive the failure of heterogeneous materials (e.g., Alava et al., 2006). Macroscopic failure arises from the nucleation and growth of fractures and faults that are influenced by heterogeneities at various scales (e.g., Lockner et al., 1991; Paterson & Wong, 2005; Peng & Johnson, 1972). In rocks, structural heterogeneities arise from grains, grain boundaries, pores, joints, and preexisting microfractures. Understanding the microscale physical laws governing the failure of crustal rocks provides fundamental insights into the characterization of precursory signals to brittle compressive failure, including microfracture propagation and arrest, and interaction of microfracture populations.

Preceding some large earthquakes, small earthquakes (foreshocks) often develop in the nucleation zone of the main shock (e.g., Bouchon et al., 2011; Jaumé & Sykes, 1999; Kato et al., 2012). However, earthquake foreshocks are not always observed (Wu et al., 2013; Zaliapin & Ben-Zion, 2013). Experimental and theoretical studies have suggested that the progressive growth of these precursors develop into unstable slip along a fault (Ohnaka, 1992).

Macroscopic brittle deformation in rocks is preceded by the propagation of precursory microfractures (Lockner et al., 1992; Wong et al., 2006). In triaxial compression laboratory experiments, microfractures tend to nucleate and localize along planar faults oriented at ~30° to the direction of the main compressive stress (Lockner et al., 1991). Optical microscopy (Moore & Lockner, 1995; Tapponnier & Brace, 1976), scanning electron microscopy (Brace et al., 1972), laser scanning confocal microscopy (Fredrich et al., 1995), and acoustic emissions (Lockner et al., 1992) have revealed some of the microstructural origins of precursors prior to macroscopic failure. Complementary to these techniques, dynamic X-ray microtomography coupled with triaxial load cell is a unique tool for imaging the microstructure of crustal rocks that are subjected to

deformation (e.g., Renard et al., 2017; Renard, Mcbeck, et al., 2019; Renard, Weiss, et al., 2018; Iglauer & Lebedev, 2017). This technique provides three-dimensional microstructural information on damage distribution as failure is approached and is complementary to other imaging techniques such as acoustic emissions (e.g., Renard, McBeck, et al., 2019).

In the present study, we analyzed in situ time-resolved three-dimensional X-ray microtomography data acquired on centimeter-scale samples of Carrara marble subjected to triaxial compression tests under stress conditions relevant for earthquake nucleation. This imaging technique produced a 3-D digital map of the spatial distribution of microfracture populations and their evolution toward failure. We developed a novel tracking algorithm to image not only the cumulated microfracture network but also the dynamics of increments of fracture growth, allowing quantifying tomography data beyond what has been previously achieved for other rocks (Renard, McBeck, et al., 2019; Renard, Weiss, et al., 2018). Our data sets provide high-resolution quantification of the dynamics of precursors prior to system-size brittle failure. Increments of fracture growth at a given stress step are related to the acoustic energies measured in some laboratory experiments and avalanches described in theoretical and numerical models of rock failure. Hence, our experimental results can test the theoretical predictions on physical laws explaining evolution of microfractures and damage (e.g., Alava et al., 2006) and explore possible deviations from scenarios of the evolution of precursor activity prior to system-size failure.

2. Background

2.1. The Microscale Origin of Rupture in Rocks: The Classical View

When low porosity rocks are loaded, microfractures may initiate from grain boundaries and internal weak zones such as fluid inclusions or healed cracks (Kranz, 1983; Paterson & Wong, 2005; Tapponnier & Brace, 1976). The Griffith's theory of fracture propagation explains failure through the propagation of cracks from preexisting defects (Griffith, 1921). Under compressive loading, it is classically considered that damage and deformation follow two phases: a first phase in which microfractures nucleate stochastically from preexisting heterogeneities in the volume and a second phase where these microfractures start interacting and grow until macroscopic failure leading to the development of roughly two-dimensional faults (Jaeger & Cook, 1969; Kuksenko et al., 1996).

At low axial stresses, rock volume variations are mostly elastic in nonporous rocks. For axial stresses above 40% to 60% of the failure stress, sample volume increases inelastically as the result of the opening of microfractures, a process called dilation (Brace et al., 1966; Hoek & Martin, 2014). Brace and Bombolakis (1963) and Hoek and Bieniawski (1965) have shown that microfractures tend to become parallel to the direction of principal stress and propagate out of their initial plane under uniaxial loading. Uniaxial and triaxial compression tests on granite showed fault surfaces with steps arranged as a staircase, and the surfaces of steps were nearly perpendicular to the direction of principal stress (Peng & Johnson, 1972). This observation was interpreted as the linkage of microfractures with orientations parallel to the main compressive stress, leading to the formation of a shear plane.

2.2. Deformation of Carrara Marble

Deformation of Carrara marble, a rock made of more than 99% calcite and composed of interlocking calcite grains, has been studied extensively. Experimental and field studies on Carrara marble in various settings have shown that macroscopic deformation is guided by microstructural changes during loading. When samples of Carrara marble were deformed near the brittle-plastic limit (Fredrich et al., 1989), a transition from localized brittle fracture to nonlocalized semibrittle flow was observed. In the semibrittle field, the stress-induced crack density and anisotropy decreased with increasing confining pressure. Crack density and anisotropy in samples deformed in the semibrittle field are comparable to those in the prefailure brittle samples. Crack density and anisotropy alone are not sufficient to characterize the damage structure that leads to localization. Fredrich et al. (1989) suggested a quantitative characterization of damage volume and its spatial correlation. Any further increase in confining pressure drove the system to the plastic domain, which inhibited microfracture growth and localization. This inhibition was interpreted by the blunting of fracture tips.

Triaxial deformation tests were performed on Carrara marble across the brittle-ductile transition (Schubnel et al., 2006), and damage growth was observed to be guided by the microstructure and rheological properties

of the rock. The same conclusion was emphasized by acoustic emission measurements (Schubnel et al., 2006). At high confining pressure, plastic strain dominated the deformation until cataclastic flow was observed (Schubnel et al., 2006). During this phase, twinning and dislocations piled up such that cracks were required to accommodate local plastic strain. When the normal stress was decreased, driving the system to a brittle regime, transient creep events was observed along with sudden growth of destabilized microcracks. Oesterling et al. (2007) analyzed the microstructures and textures of a natural shear zone in Carrara marble sampled in the upper part of the Frigido valley in the central Alpi Apuane, Italy. They observed that deformation in this natural shear zone showed strain-dependent variations in microstructure. In the present study, we consider deformation of Carrara marble in the brittle regime and present microstructural changes during deformation, which may provide insights in understanding deformation in this natural shear zone.

2.3. Fracture and Damage Models of Failure

Heterogeneities and disorder guide fracture nucleation and propagation in rocks and other heterogeneous brittle materials. Prior to macroscopic failure, precursory activity was observed as the progressive nucleation of microfractures and their stable growth (Lockner et al., 1992; Renard, Weiss, et al., 2018; Vu et al., 2019; Wong et al., 2006).

Empirical failure criteria, such as the Mohr-Coulomb criterion, quantify rock strength (e.g., Paterson & Wong, 2005). However, by construction, these approaches do not consider the existence of precursors. More recently, theoretical models were developed to describe failure in heterogeneous media, such as rocks, using concepts from out-of-equilibrium statistical physics. These models consider long-range stress interactions and disorder and history effects during loading (e.g., Alava et al., 2006). In these models, heterogeneities in the system are described by a spatial distribution of local stress threshold or initial defects with varying elastic parameters. During loading, damage evolution is inferred from the spatial organization of damage events and energy dissipation that accounts for the complex interplay between disorder and elastic interaction of microfractures. In such models, failure can be described as a phase transition from an initial unbroken stage to a final broken stage (e.g., Alava et al., 2006; Dahmen et al., 2009; Girard et al., 2012; Vu et al., 2019). Evolution of damage is tracked in terms of a control parameter, which is a measure of the applied load.

In the present study, we imaged and measured the total damage volume, the increments of damage, and the volume of the largest microfracture cluster as Carrara marble specimens approached failure. Our main goal is to quantify the relationships between these parameters and the applied stress by using the reduced control parameter, $\Delta_D = \left(\sigma_D^f - \sigma_D\right)/\sigma_D^f$, where σ_D is the differential stress applied on the sample and σ_D^f is the differential stress at failure, considered here as the critical point where the failure transition occurs.

In Figure 1, we summarize the various parameters used in the present study and represent how microfracturing controls the road to failure. Numerical simulations that consider rock failure as a critical phase transition predict that these parameters should follow power law behavior with well-defined exponents when approaching failure (Girard et al., 2012). We compare the scaling exponents measured in our experiments with theoretical predictions and experimentally test the critical nature of the failure process, providing new insights into the failure of geomaterials. We quantify how long-range interactions and disorder present in the system guide the route to brittle compressive failure in Carrara marble.

3. Material and Methods

3.1. Experimental Procedure

Carrara marble, a rock made of 99.6% of calcite, with very low porosity close to ~0.2% and grain sizes in the range 100–200 μm (Rutter, 1972; Malaga-Starzec et al., 2002), was deformed. Two cylindrical samples, 10-mm height and 5-mm diameter, were cored from the same $10 \times 10 \times 10$-cm block. We used an experimental technique that couples high-resolution synchrotron X-ray microtomography and the Hades triaxial deformation apparatus (Renard et al., 2016), enabling time-lapse three-dimensional imaging of rocks at in situ conditions of stress during deformation. We tracked the evolution of fractures in two specimens of Carrara marble (labeled M8-1 and M8-2) that were deformed until brittle failure (Table 1). Each specimen was mounted in the triaxial deformation apparatus ($\sigma_1 > \sigma_2 = \sigma_3$) as shown in the inset of Figure 2. The Hades apparatus is installed on the rotating stage of the X-ray microtomography beamline ID19 at the

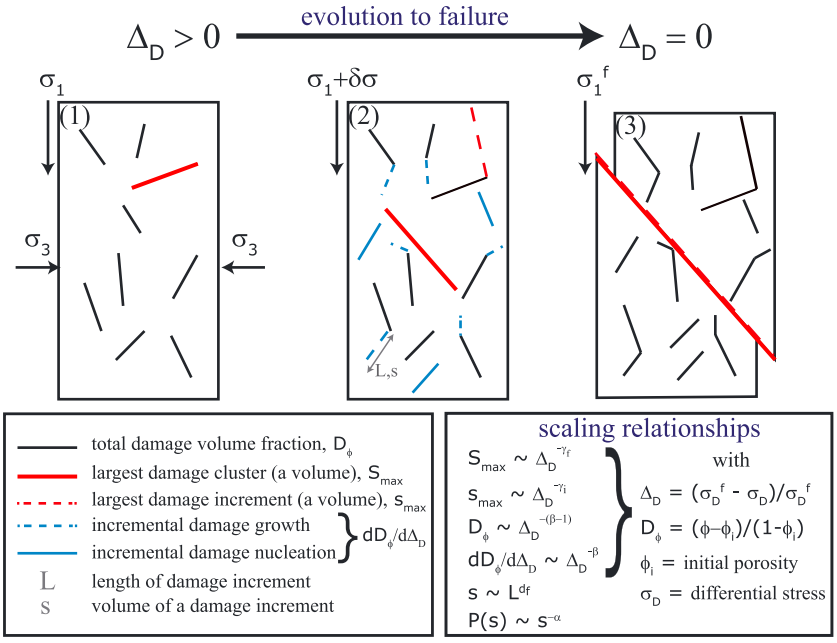

Figure 1. Sketch showing the evolution of Carrara marble toward macroscopic failure in three stages of deformation: (1) random nucleation of microfractures; (2) nucleation, growth, and localization of damage increments; and (3) development of a shear fault at failure. σ_1: axial stress, $\sigma_3 = \sigma_2$: confining pressure, $\sigma_D = (\sigma_1 - \sigma_3)$: differential stress, σ_D^f: differential stress at failure, $_D$: stress control parameter. If failure is considered as a critical phenomenon (Girard et al., 2012; Vu et al., 2019), several power law scaling relationships should emerge among stress control parameter, $_D$; the cumulative microfracture (black line) volume fraction quantified by the damage parameter, D_φ; the volume fraction of the largest microfracture cluster, S_{max} (red line); the volume fraction of damage increments (blue dotted and solid lines); the volume fraction of the largest damage increment, s_{max} (red dotted line), dD_φ/d_D; the size (volume), s, and length, L, of a given microfracture increment; and the probability distribution of damage increments, $P(s)$. γ_f, γ_i, d_f, β, and α are the power law scaling exponents. d_f is the fractal dimension of microfracture increments.

European Synchrotron Radiation Facility (Grenoble, France). Each sample was loaded axially between stainless steel pistons. The interfaces between the pistons and the sample were not lubricated. The sample was inserted into a polymer jacket, and silicon oil applied a constant confining pressure to the sample. Experiments were performed at 25 °C, without pore fluid. The presence of a high flux of X-rays during the scans did not modify the internal temperature in the rig, which was monitored with a thermocouple.

During the experiments, the axial stress was increased in successive steps of either 2 MPa (sample M8-1) or 1 MPa (sample M8-2), until failure. At every step increase in stress, a three-dimensional X-ray microtomography volume was recorded with 2,500 radiographs per scan, with a rotation of 180 degrees. Radiographs were acquired with a polychromatic X-ray beam (Wiggler gap of 68 mm with 5.6 mm of Al filter), given an equivalent energy of 85 keV that crossed the sample. The pixel size was 6.5 μm. Each scan lasted 90 s during which the applied stress was held constant. At this resolution, we did not detect any blurring artifact indicating movement of the sample or fracture growth during scan acquisition. During a single-stress increase, microfractures nucleated, coalesced, or closed by a single growth event or by successive events of growth that occurred during this stress step increase.

Table 1
Experimental Conditions for the Deformation of the Two Carrara Marble Samples

Sample	Confining pressure	Differential stress at yield	Differential stress at failure	Temperature	Rate of increase in differential stress	Number of 3-D scans
M8-1	20 MPa	88 MPa	100.7 MPa	25 °C	2 MPa/step	44
M8-2	25 MPa	126 MPa	156.8 MPa	25 °C	1 MPa/step	97

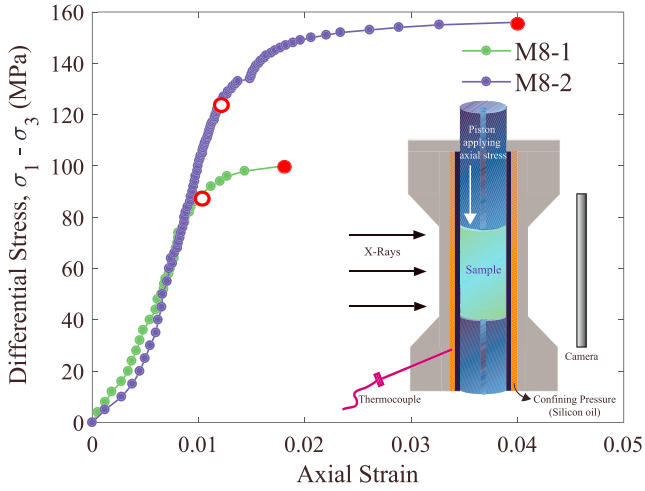

Figure 2. Axial strain versus differential stress for Carrara marble samples M8-1 (confining pressure of 20 MPa) and M8-2 (confining pressure of 25 MPa). Both samples exhibited a quasi-brittle failure behavior. Each circle corresponds to the acquisition of a three-dimensional X-ray tomography volume. Open red circle: macroscopic yield point. Full red circle: last X-ray tomography scan before failure. Inset: sketch of the Hades rig.

Series of 44 and 97 dynamic X-ray microtomography volumes were acquired for samples M8-1 and M8-2, respectively. The radiographs were reconstructed in three dimensions using plain filtered back projection (Mirone et al., 2014), coupled with a single-distance phase retrieval algorithm adapted from Paganin et al. (2004). After experiments, the specimens were impregnated with liquid epoxy resin and then cut along the axial plane after the liquid epoxy had solidified. The exposed surface was polished, coated with 10-nm gold, and imaged using a Hitachi SU5000 scanning electron microscope at the University of Oslo, with a voltage of 15 kV.

3.2. Segmentation of the Tomograms

As the specimens deformed toward failure, damage accumulated in their volume as nucleating and propagating microfractures. The series of three-dimensional digital volumes obtained at every stress step until deformation were postprocessed to extract this damage. The 3-D tomograms were 16-bit images that included artifacts such as rings, periodic stripes, and speckle noise. Seven steps were followed to extract the evolution of damage with increasing stress:

1. Periodic stripes on every 2-D slice appeared due to the noise from the scintillator. A Fourier transform of each original 2-D slice was calculated, and the part of the spectrum that corresponded to higher intensities was cut off to remove these stripes. The inverse Fourier transform of the image was then calculated to recover the original slice (Figure 3a).

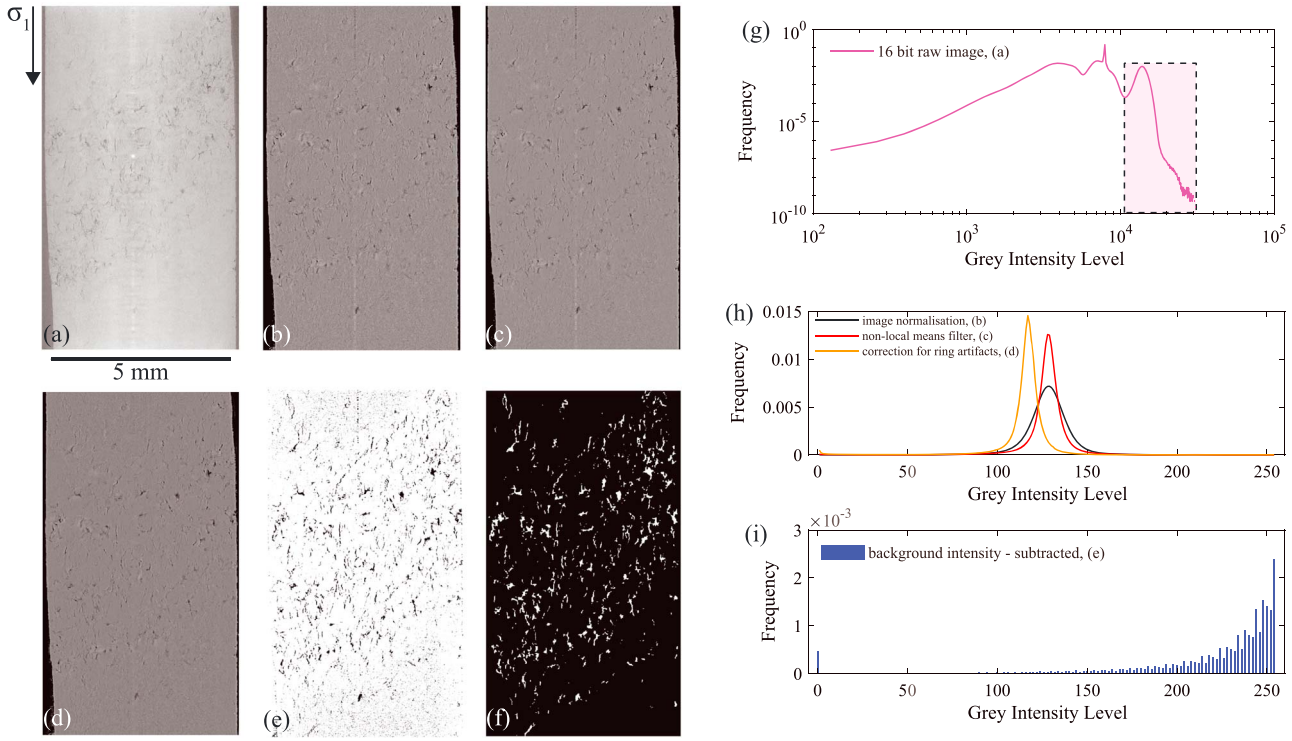

Figure 3. Two-dimensional sections of a three-dimensional volume at various steps of the data segmentation process used to extract the microfractures. (a) Initial reconstructed 16-bit image and (g) corresponding grayscale histogram. Region shaded in pink corresponds to the rock, while the rest of the histogram corresponds to the jacket and oil used for confining the sample. (b) Normalization of the grayscale histogram and transformation into 8-bit image. (c) Image after applying a nonlocal means filter. (d) Image corrected for ring artifacts and corresponding histograms shown in (h). (e) Image after background intensity was subtracted and (i) corresponding histogram. (f) Segmented image with the microfractures in white.

2. The gray level in each volume was normalized to enhance the details of the microfractures (Figure 3b) and saved into 8 bit.
3. A nonlocal means filter (Buades et al., 2005) was applied to average out the speckle noise and sharpen the microfractures (Figure 3c).
4. We used a Matlab package for ring artifact correction (Jha et al., 2014) to remove these artifacts in the three-dimensional volumes. A resulting image is shown in Figure 3d.
5. We employed a background subtraction algorithm (Sternberg, 1983) to remove a smooth continuous background across the image (Figure 3e). This step is performed by choosing a "rolling ball" radius for each image. At every voxel is assigned a local background value by averaging around the voxel over of the rolling ball. This averaged intensity is subtracted from the original image. To remove large spatial variations in the background intensity, we have used the background subtraction filter of the software AvizoFire.
6. Each image was then thresholded to select microfractures. Varying slightly this threshold did not change quantitatively the results (Figure S2 in the supporting information). Microfractures with a volume less than 100 voxels were limited by the resolution of the segmented images and were removed. Therefore, the value of 100 voxels is the lower limit of microfracture size considered here. At the end of this last segmentation step, we obtained a binary image with microfractures quantified as intensity value 1 and the rock with intensity value 0 (Figure 3f).
7. Finally, we have used dilation-erosion filtering to connect voxels that belong to the same microfracture. The procedure we used was to dilate the microfractures by one voxel to connect close neighbors and then erode these microfractures by one voxel to recover their original volume.

3.3. Microfracture Statistics

Geometric characteristics of microfractures such as position, volume, surface area, and shape parameters were calculated from the segmented binary three-dimensional data. Because microfractures accumulated at every axial stress step increase, σ_j, each microfracture or microfracture network at this stress step resulted from the cumulative growth of preexisting microfractures or nucleation of new microfractures that formed during the stress steps $\sigma_{j=1}$ to σ_j (Figure 1). We observed that the incremental damage volume at step σ_j results from a balance between the growth of preexisting fractures, the nucleation of new ones, and the possible closing of some of the preexisting microfractures, whose total volume is negligible (Figure S5). We distinguished between the cumulated damage, D_φ, defined as the total microfracture volume fraction at a given stress step σ_j, and the incremental damage, $\mathrm{d}D_\varphi/\mathrm{d}\Delta_D$, between each stress step σ_{j-1} to σ_j. In order to obtain an instantaneous measurement of the progressive growth of damage, we computed the dynamic variable, the damage increments s that formed only between stress steps σ_{j-1} and σ_j. The sum of these increments s normalized by the sample volume gives the incremental damage, $\mathrm{d}D_\varphi/\mathrm{d}\Delta_D = \frac{\sum_{\sigma_j} s}{V_j^{\mathrm{sample}}}$ for a given stress step σ_j, and sample volume V_j^{sample}. These damage increments, s, between two successive stress steps were extracted by mapping the segmented volume V_{j-1} at the $(j-1)$th stress step with the consecutive volume V_j at the next stress step such that the position of every voxel in volume V_j has a corresponding position in the volume V_{j-1}. We could then select voxels that corresponded to new increments of damage in the volume V_j compared to the volume V_{j-1}. This mapping was necessary because the sample may have compacted or dilated between successive stress steps, so that a simple difference between successive three-dimensional tomograms cannot be used to extract damage increments. This procedure provides new ways of quantifying damage in tomography data, which could not be performed in previous studies (Renard, McBeck, et al., 2019; Renard, Weiss, et al., 2018).

The centroids and volumes of damage increments at every step were tracked until failure and sorted into three categories: (1) damage increments that grew and propagated between stress steps $(j-1)$ and j (blue dashed lines in Figure 1), (2) nucleation of new microfractures at stress step j (full blue lines in Figure 1), and (3) closing or coalescence of microfractures from steps $(j-1)$ and j (Figure S1). The large numbers of microfractures and microfracture increments enable robust statistical analysis on the damage and damage increments. In the analysis, the stress step σ_j is translated in terms of the control parameter, Δ_D. An example of the results obtained using this algorithm is shown in Figure S1.

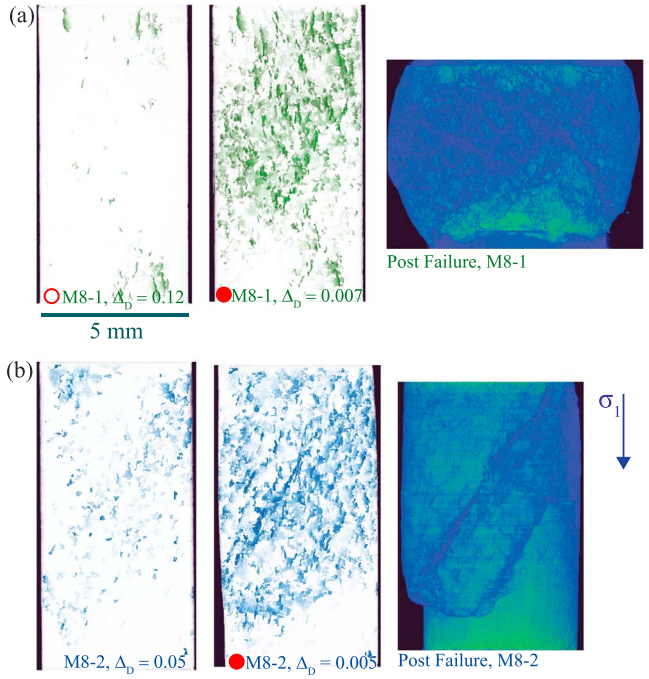

Figure 4. View of segmented damage (i.e., microfractures) in samples M8-1 (a) and M8-2 (b). The left image displays the damage at the macroscopic yield point. The middle image shows the damage at the onset of failure, and the right image shows a three-dimensional rendering of sample after failure and slip along shear planes. Open red circle shows the macroscopic yield point; full red circle shows the last scan acquired before failure for which the corresponding distance to failure $_D$ is indicated. Animations of the evolution of damage are provided in the supporting information (Movies S1–S3).

3.4. Advantages and Limitations of the Experimental Technique

A crucial advantage of the present experimental technique is that all damage can be detected within the spatial resolution, independently of how this damage was produced by a dynamic crack propagation (i.e., seismic) or by a slow crack propagation (i.e., aseismic). Moreover, the exact spatial location of the damage in the sample is unambiguous in our data, which also give access to the shape and orientation of the microcracks (see section 4.3 below and Renard, McBeck, et al., 2019; Renard, Weiss, et al., 2018). These are important differences with experimental studies that monitor damage evolution using acoustic emissions.

On the other hand, the X-ray microtomography experimental technique employed in the present study has several limitations. First, because each scan must be performed on a sample that does not deform, the stress must be maintained constant during each acquisition. The consequence is that despite the loading path is performed at an average constant strain rate, stress is increased step by step. In average, the strain rate was low enough to avoid subcritical crack propagation; therefore, we consider that this experimental constraint did not affect the overall brittle behavior of the samples.

Another limitation is the spatial resolution of 6.5 μm that does not allow detecting microfractures smaller than this resolution. Because our study is based on the detection of voids (i.e., volumetric damage), we cannot detect preexisting microfractures that would have slid during a given stress step increase, without producing additional damage or local dilation. Such situation would happen likely for slips below the spatial resolution of the data.

4. Results

As the differential stress was increased, the deformation of the Carrara marble samples can be qualitatively characterized by the progressive accumulation of damage, which finally localized along a shear plane resulting in a macroscopic fault (Figures 1, 2, and 4). Damage accumulated by an increase in the number and size of microfractures, which dilated the volume. Because we could extract the microfractures visible at the resolution of the tomograms, we were able to quantify the statistical evolution of six parameters as a function of the control parameter, $\Delta_D = \left(\sigma_D^f - \sigma_D\right)/\sigma_D^f$, at failure (Figure 1), as mentioned in section 2.3. We tracked the following:

1. the total damage volume fraction defined as $D_\varphi = \frac{\phi-\phi_i}{1-\phi_i}$, where ϕ is the volume fraction of all open microfractures and voids at a given stress step and ϕ_i is the volume fraction corresponding to the initial porosity of the sample before loading ($\phi_i \approx 0.2\%$);
2. the new volumes of voids and microfractures, also called incremental damage, with increasing differential stress, $dD_\varphi/d\Delta_D$, computed as explained in section 3.3.
3. the volume fraction of the largest microfracture cluster, S_{max};
4. the volume fraction of the largest damage increment s_{max};
5. the size (volume) s and the largest eigenvalue of microfracturing increments, considered as their lengths L; and
6. the probability distribution of microfracture increments, $P(s)$.

All these parameters are sketched in Figure 1. Their evolution toward the peak stress should show power law scaling if brittle failure is a critical phenomenon (Girard et al., 2012). Two procedures may be used to obtain the scaling exponents (Stanley, 1999). We present the first method in section 4.2 by calculating scaling laws. We present the second method in section 4.3 by performing a data collapse analysis.

4.1. Macroscopic Mechanical Behavior and Microstructure

Here, we analyze the macroscopic failure in Carrara marble along with the microstructural changes. Figure 2 displays the macroscopic mechanical behavior of the two specimens. The differential stress-axial strain response was nonlinear for differential stresses below 40 MPa. We interpret this behavior to arise from the closure of voids during initial loading. A quasi-linear regime was observed above 40 MPa until a significant departure from elastic behavior occurred, here defined as the macroscopic yield stress, σ_D^y. The position of this yield stress occurs at a deviation of linearity in the effective stress versus volumetric strain curve (Brace et al., 1966). This point nearly occurs at 90% and 80% of the differential stress at failure, σ_D^f, for samples M8-1 and M8-2, respectively (Table 1). After this point, additional increases in differential stress resulted in irreversible macroscopic strain deformation until σ_D^f was reached, where an abrupt transition to macroscopic brittle failure was observed. Within one-step increase in applied differential stress, the rocks failed and a stress drop larger than 10 MPa occurred. Figure 4 shows views of the total damage, D_φ, at the yield point and near failure, as well as 3-D renderings of the failed samples, and indicates that damage started well before the macroscopic yield.

Tomography data show that damage clusters initially nucleated in spatially disperse, apparently random, locations in the initial stage of deformation (Movie S1), similar to acoustic emissions locations in granite (Lockner et al., 1991). With increasing differential stress, microfractures localized near the largest damage clusters (Movie S1), growing into larger clusters (Movie S2), until one or few quasi two-dimensional system-spanning shear planes developed (Movie S3). The shear planes were oriented at $30° \pm 3°$ to the direction of the main compressive stress, σ_1, as shown in Movies S1 and S3. Figure 4 shows snapshots of segmented microfractures in both samples (Movie S1) and the sample configuration after failure, which corresponds to the last snapshot in the Movie S3.

Figure 5 shows scanning electron microscopy images of the samples after deformation. The mean grain size was in the range 100–200 μm, in agreement with other studies (Rutter, 1972; Malaga-Starzec et al., 2002). A larger number of microfractures grew within grains rather than along grain boundaries (Figure 5e). Their general orientation tended to be roughly parallel to the main compressive stress direction (Figure 5b). Some microfractures also propagated across grain boundaries. After failure, damage localization resulted in several shear planes (Figures 5c and 5d), which were oriented at an angle of ~30° to the main compressive stress. Shear sliding resulted in cataclasis and reduction in grain size along with the formation of a gouge (Movies S1 and S3).

4.2. Damage Scaling Laws

Data allow computing geometrical parameters of microfractures. The dynamics of microfractures toward system-size failure was tracked as a function of the control parameter, Δ_D, which measures the distance to failure through the applied differential stress. We also represent the evolution of the damage parameter, D_φ, as a function of normalized differential stress σ_D/σ_D^f (Figure 6). Microfractures nucleated and grew, producing macroscopic irreversible strain (Figure 2). An accelerated growth of D_φ toward failure was observed (Figure 6). For sample M8-1, a sharp increase of D_φ was observed when approaching failure. However, due to the limited number of tomograms near failure, a robust fit could not be estimated for this sample. For sample M8-2, for which more three-dimensional volumes were acquired when approaching failure, the growth of D_φ was progressive and accelerated toward failure. In the range $0.02 < \Delta_D < 0.2$, this acceleration followed a power law $D_\varphi \sim {\Delta_D}^{-(\beta - 1)}$ with an exponent $(\beta - 1) = 1.5$ (inset of Figures 6 and S3). Here the exponent $(\beta - 1)$ comes from the fact that the exponent β is defined for the incremental damage, $dD_\varphi/d\Delta_D$, for which we expect a power law acceleration $\mathrm{d}D_\varphi/\mathrm{d}\Delta_D \sim {\Delta_D}^{-\beta}$ (see Renard, McBeck, et al., 2019; Renard, Weiss, et al., 2018, and below), while the total damage, D_φ, is the integral of this quantity (Figure 1). For this sample, D_φ tapered at small values of the control parameter and showed an exponential evolution for $\Delta_D < 0.02$.

Microtomography data provide information on the volume of microfractures from the beginning of the experiment. In order to compare our results with existing theoretical and numerical studies on brittle failure, we have computed the change in the volume of pores and microfractures, $\mathrm{d}D_\varphi/\mathrm{d}\Delta_D$, between two successive stress steps (see section 3.3). The evolution of $\mathrm{d}D_\varphi/\mathrm{d}\Delta_D$ during loading is relevant to compare our experimental results with theoretical models of damage progression toward failure (Alava et al., 2006; Girard et al., 2012).

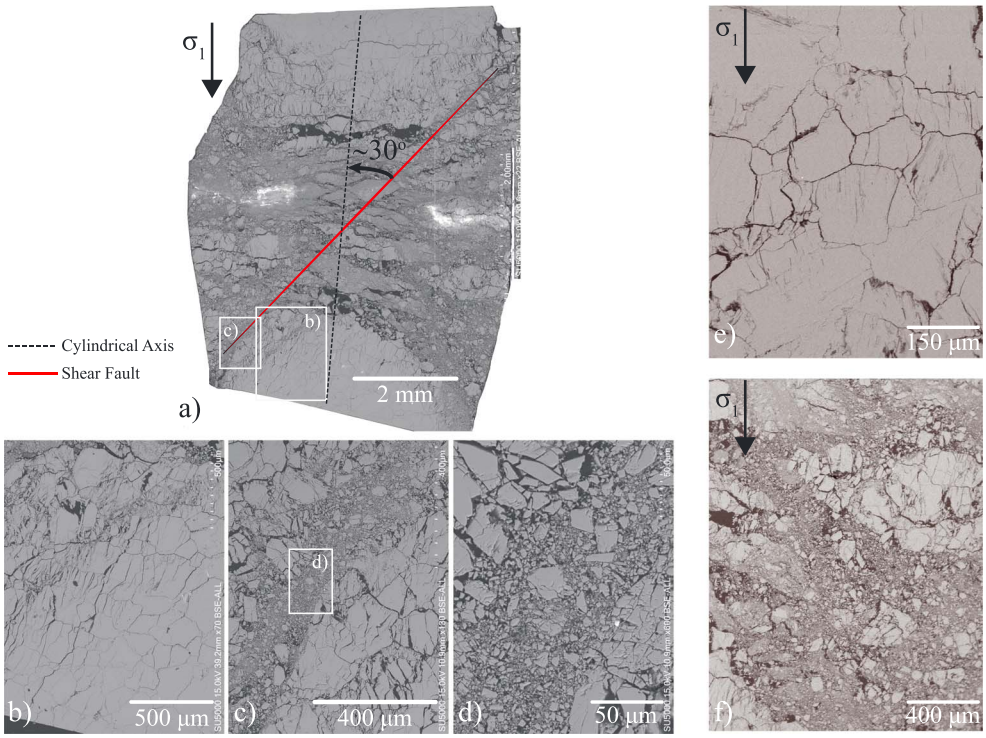

Figure 5. Scanning electron microscopy images of samples M8-1 (a–d) and M8-2 (e, f) recovered after failure. (a) Vertical cross section in the middle of the entire sample. (b–d) Zooms showing microfractures in grains (b) and zoom on one shear zone with intense grain comminution (c, d). (e) Development of microfractures inside grains and opening of grain boundaries. Many intragranular microfractures are pinned at grain boundaries. (f) Shear zone in sample M8-2 with intense grain comminution. In all images, the main compressive stress is oriented vertical.

These theoretical models have predictions for volume fractions of $dD_\varphi/d\Delta_D$ produced by the damage nucleation and growth and are plotted as a function of Δ_D in Figure 7a for sample M8-2. These data show that the growth of existing microfractures in the neighborhood of large microfractures is dominant in number and volume compared to the nucleation of new microfractures when approaching failure. For sample M8-2, $dD_\varphi/d\Delta_D$ shows a power law scaling $dD_\varphi/d\Delta_D \sim \Delta_D^{-\beta}$ up to the vicinity of failure ($\Delta_D \approx 2 \times 10^{-2}$) with an exponent $\beta = 2.6$ fully consistent with the results of Figure 6 for cumulated damage ($\beta - 1 = 1.5$) (inset in Figure 7a). A tapering of the power law behavior of $dD_\varphi/d\Delta_D$ for $\Delta_D < 0.02$ is observed, similar to the flattening or exponential increase observed in the behavior of D_φ (Figure 6).

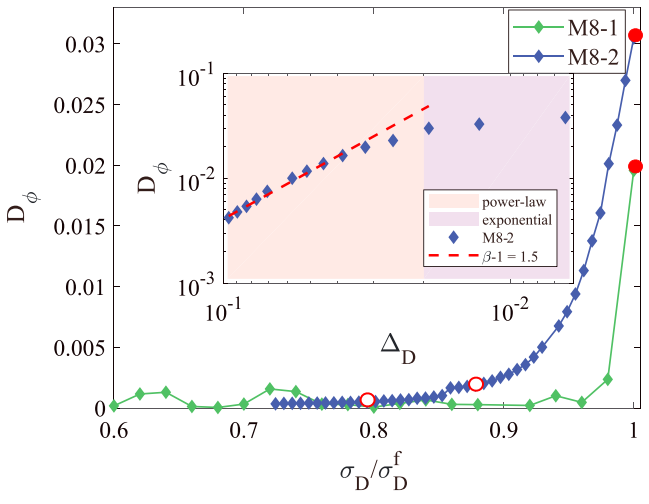

Figure 6. The damage index, D_φ, increases with increasing differential stress for samples M8-1 (green) and M8-2 (blue). Inset: log-log plot of D_φ as a function of $_D$ for sample M8-2. A linear trend in the range $0.02 < _D < 0.1$ demonstrates a power law relationship $D_\varphi \sim _D{}^{-(\beta - 1)}$ with a scaling exponent $(\beta - 1) = 1.5$. Open red circle shows the macroscopic yield point; full red circle shows the last scan acquired before failure.

We also computed the number of damage increments between two successive stress steps, $dN/d\Delta_D$, also called damage event rate. In seismology, it has been proposed, for example, that volcanic eruptions could be preceded by an accelerating foreshock sequence following a so-called inverse Omori's law, $dN/dt \propto (t_f - t)^{-p}$ (e.g., Bell et al., 2013), with N the number of earthquakes. In our system, we consider an equivalent inverse Omori's law, $dN/d\Delta_D \propto \Delta_D{}^{-p}$, where time is replaced by the control parameter Δ_D. The number of damage increments plotted as a function of Δ_D for sample M8-2 (Figure 7b) follows such inverse Omori law until $\Delta_D \approx 0.02$ with a scaling exponent $p = 1.9 \pm 0.05$. Breaking down of this inverse Omori scaling close to failure, for $\Delta_D < 0.02$, could possibly be connected to the tapering of the power law behavior of $dD_\varphi/d\Delta_D$ shown in Figure 7a.

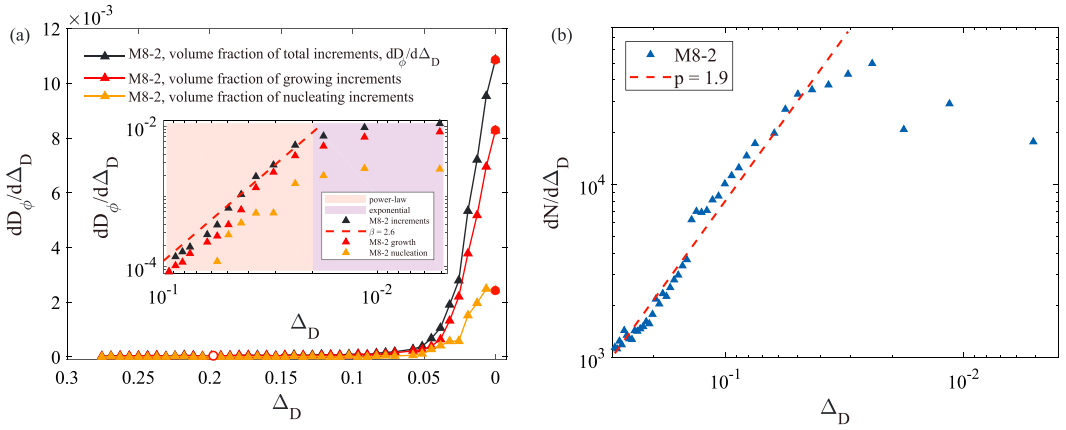

Figure 7. (a) Evolution of incremental damage, dD_{φ}/d_D as a function of control parameter, $_D$ in sample M8-2. Damage increments are tracked as incremental events of growth and nucleation (see Figure 1), and the respective volume fractions are plotted as a function of $_D$. Inset: Rate of damage growth and nucleation plotted against control parameter for sample M8-2, showing a scaling $dD_{\varphi}/d_D \sim {}_D^{-\beta}$ with an exponent $\beta = 2.6$ for $0.02 < {}_D < 0.1$ (red dashed straight line). For $_D < 0.02$, an exponential evolution is observed. Open red circle shows the yield point; full red circle shows the last scan acquired before failure. (b) Number of damage increments (damage event rate), dN/d_D plotted as a function of control parameter, $_D$, shows a power law scaling, $dN/d_D \sim {}_D^{-p}$ with exponent $p = 1.9 \pm 0.06$ for $_D > 0.02$ and a fluctuating decrease for $_D < 0.02$.

When approaching failure, the dynamics of microfractures was dominated by the growth of the largest microfracture, S_{max}, defined as the volume fraction of the largest microfracture cluster. Figure 8 shows the growth of the largest cluster, S_{max} and of largest increment, s_{max}, as a function of Δ_D. The volume fraction of the largest cluster in sample M8-1 remained very small prior to failure and increased abruptly at failure. Once again, the number of scans before failure is too limited for this sample to precisely track the evolution of S_{max} or s_{max}. For sample M8-2, where the rate of loading was slower, it was possible to track the growth of the largest cluster prior to the peak load in more details (inset in Figure 8). It showed a power law scaling, $S_{max} \sim \Delta_D^{-\gamma_f}$, with an exponent $\gamma_f = 2.4 \pm 0.1$. At failure, the largest cluster occupied 1.5% and 1.9% of the total microfracture volume in M8-1 and M8-2, respectively, and connected the two opposite boundaries of the sample. The volume fraction of the largest damage increment, s_{max}, plotted against the control parameter showed a similar power law scaling, $s_{max} \sim \Delta_D^{-\gamma_i}$, with a smaller exponent $\gamma_i = 1.1 \pm 0.1$ for sample M8-2 (inset in Figures 8 and S4). Within the inherent fluctuations in the evolutions of S_{max} and s_{max} (see inset of Figure 8), we did not detect a significant breaking of scaling near final failure in this case.

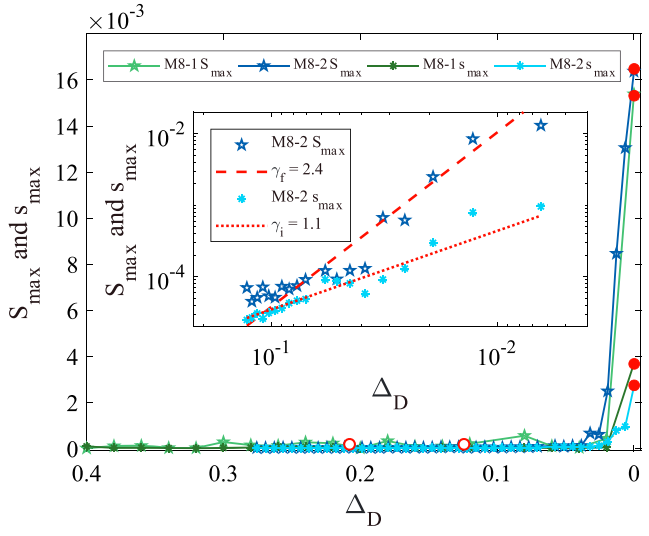

Figure 8. Volume fractions of the largest microfracture, S_{max}, and of largest increment, s_{max},plotted against the control parameter, $_D$, for both samples, M8-1 (green) and M8-2 (blue). Inset: log-log plot of S_{max} and s_{max} as a function of $_D$ showing a power law scaling, $S_{max} \sim {}_D^{-\gamma_f}$ and $s_{max} \sim {}_D^{-\gamma_i}$ for sample M8-2, with exponents, $\gamma_f = 2.4 \pm 0.1$ and $\gamma_i = 1.1 \pm 0.1$ (Figure S4). Open red circle shows the macroscopic yield point; full red circle shows the last scan acquired before failure.

4.3. Shape and Size Distribution of Damage Increments

To characterize the shape of the fracture increments, we calculated their size (volume), s, and maximum length, L, computed as the largest eigenvalue of the covariance matrix. This eigenvalue may interpreted as representing the largest axis of the best fit ellipsoid of a given microfracture. A power law scaling, $s \sim L^{-d_f}$, where d_f is the fractal dimension characterizing their shape, was observed with d_f=2.3 and 2.1 for samples M8-1 and M8-2, respectively (Figure 9). The value of these exponents, close to 2, indicates that the fracture increments are quasi-two-dimensional objects, as expected for microfractures.

Figure 10 shows the cumulative density functions (CDF) of damage increment sizes occurring at different stress steps, corresponding to different

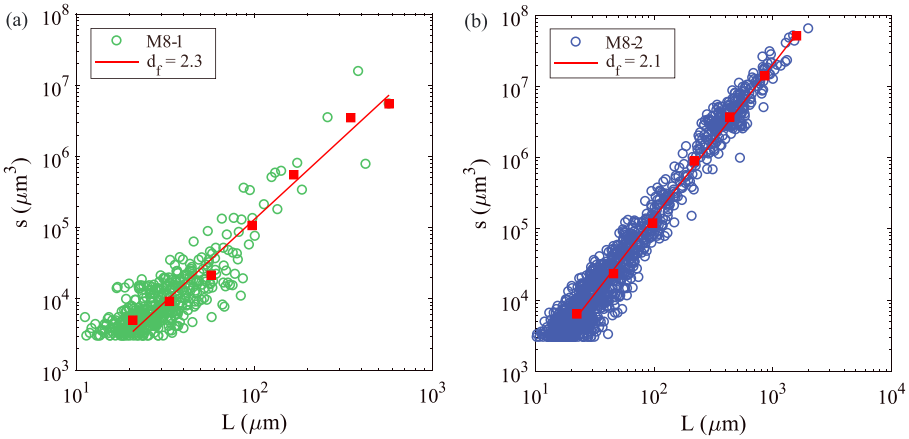

Figure 9. Size (volume) of damage increments, s, plotted against their lengths L for samples M8-1 (a) and M8-2 (b). Red squares represent average sizes of binned data. The fractal dimension d_f in both cases is 2.2 ± 0.8, showing that damage growth increments were quasi-planar two-dimensional objects, corresponding to microfractures.

values of the control parameter Δ_D, for samples M8-1 (Figure 10a) and M8-2 (Figure 10b). Several important features can be identified as follows:

1. For sizes (volumes) larger than ~10^5 μm^3, the CDFs progressively evolve toward a power law distribution, $P(\geq s) \sim s^{-\alpha+1}$, as one approaches the failure stress.
2. This power law scaling is clearly broken down at a lower cutoff, $s_{inf} \approx 10^5$ μm^3. As $s \sim L^{-d_f}$ (Figure 9), this translates into a cutoff length scale $L_{inf} \approx 10^{5/2.2} \approx 180$ μm. This value, which fits very well with the range of grain sizes of Carrara marble (100–200 μm), illustrates the role of grain boundaries as barriers to microfracture extension. Microfractures confined within individual grains clearly differ from the damage dynamics and interactions at larger scales.
3. At the ultimate stress steps before final failure, some outliers are visible in the tail of the distributions, corresponding to anomalously large damage increments. The physical interpretation of these outliers is discussed in section 5.3.

From the results of point (1), we conjecture (for scales larger than the average grain size, see point [2]), an evolution of the probability density function (PDF) of damage increment sizes of the form, $p(s) \sim s^{-\alpha} f(s/s^*)$, where $f(x)$ is a rapidly vanishing function for $x > 1$ and the upper cutoff, s^*, grows toward the failure stress as $s^* \sim \Delta_D^{-\gamma}$. This conjecture is consistent with a nontruncated PDF near failure, $P(s) \sim s^{-\alpha}$ (or equivalently

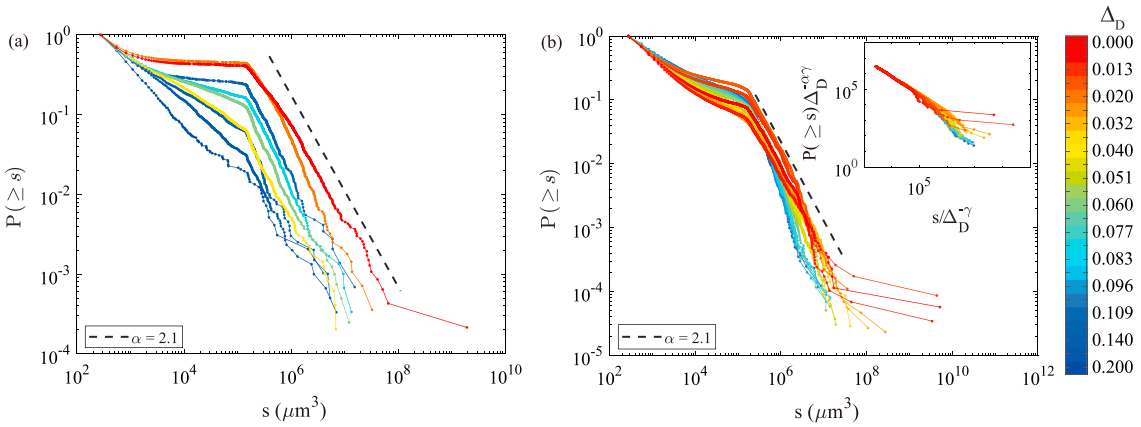

Figure 10. Cumulative density functions of the sizes of damage increments, $P(\geq s)$, for (a) samples M8-1 and (b) sample M8-2, for different stress steps, that is, different values of $_D$. Inset: Data collapse of the data of sample M8-2. The slope breaking in the data around microfractures sizes of 10^5 μm^3 corresponds to the average grain size of the rock (see text for details).

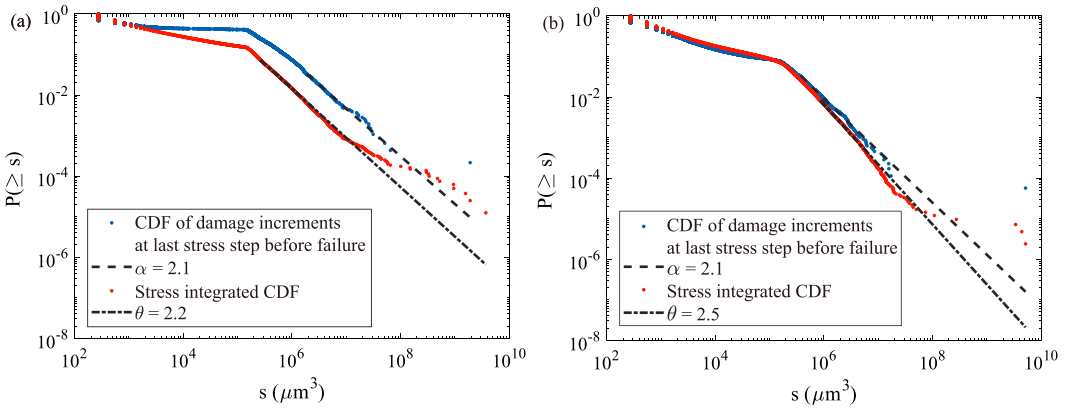

Figure 11. Cumulative density functions (CDF) of the sizes of damage increments at the last stress step before failure and CDF of stress-integrated (damage increments recorder over the entire loading up to peak stress) distributions for (a) samples M8-1 and (b) sample M8-2.

$P(\geq s) \sim s^{-\alpha+1}$ for the CDF); see Figure 10, as the cutoff volume, s^*, spans the entire volume of the system. In addition, the stress-integrated (damage increments recorder over the entire loading up to peak stress) PDF should follow another nontruncated power law, $P(s) \sim s^{-\theta}$, with $\theta = \alpha + 1/\gamma$ (Sornette, 1994). Our results for the sample M8-2 support this conjecture with $\alpha = 2.1 \pm 0.4$ and $\theta = 2.5 \pm 0.07$; hence, $\gamma = 2.5 \pm 2.5$ (Figure 11b). We have used a robust maximum likelihood method (Clauset et al., 2009) to estimate the power law exponents. Because of the propagation of errors, the uncertainty on γ is large. This value can however be confirmed from a data collapse analysis. Using the values of α and γ, the CDFs of Figure 10b can be collapsed by plotting $P(\geq s) \sim \Delta_D^{-\alpha\gamma}$ as a function of $s/\Delta_D^{-\gamma}$, as shown in the inset of Figure 10b. From this scaling of the upper cutoff, s^*, the evolution of the correlation length of damage dynamics, ξ, can be obtained from the fractal scaling of damage increments (Figure 9), that is, $\xi \sim \left(s^*\right)^{1/d_f} \sim \Delta_D^{-\nu}$, with $\nu = \frac{\gamma}{d_f} = 1.15$.

Note that, for sample M8-1, although we observed a reasonable power law distribution for the last scan before failure as well as for the stress-integrated distribution (Figure 11a), with $\theta > \alpha$, the estimation of γ was not reliable, most likely because of the limited number of scans before failure (last scan too far from failure).

Finally, we would like to stress that we compare in the present study two experiments, performed at two different stress and strain rate resolutions (value of stress steps and number of scans to failure). Although the experiment M8-1 does not allow a precise characterization of the acceleration of damage as approaching failure, the two experiments (M8-1 and M8-2) are consistent in terms of largest microfracture and largest increment (Figure 8), shape of damage increments (Figure 9), and distribution of damage increment sizes (Figure 11). Therefore, we consider that, despite a different resolution in the two experiments, results on the evolution of the microstructure prior to failure show the same quantitative behavior.

5. Discussion

5.1. Microstructural Changes as Approaching Failure

In our experiments, we observed sample compaction at the very early stages of deformation (Figures 5c, 5d, and 5f). Above the yield point, the samples dilated with increasing load. Our results allow linking this macroscopic process to the nucleation and growth of microfractures. The samples deformed through the formation of microfractures that increased in number and volume. When approaching failure, the number of fracture clusters decreased due to microfracture coalescence, while the volume of the largest cluster and the total damage increased (Figure 6). Therefore, in the last stages of deformation, the growth of preexisting microfractures dominated the nucleation of new ones (Figure 7). We observed the development of intragranular microfractures parallel to the axial stress direction (Figure 5). After failure, sliding occurred along system-spanning faults (Figure 4 and Movie S3). A further increase of the differential stress promoted further

frictional sliding and considerable decrease in sample height (last frame of Movie S3). This frictional sliding induced a reduction of grain size (grain crushing) along the shear faults (Figure 5).

Our results are consistent with other studies on the deformation of Carrara marble under uniaxial or triaxial compressive stress conditions (Tal et al., 2016; Wawersik & Fairhurst, 1970; Wong & Einstein, 2009). Two-dimensional strain maps obtained from uniaxial tests on marble (Tal et al., 2016) were decomposed into shear and normal components. The normal and shear components of strain were localized along narrow and diagonal features interpreted as microfractures. These shear and dilatant features coalesced with increasing load, increasing in density. Near yield, dilatant vertical microfractures initiate along the grain boundaries that result in a decreasing slope of the stress-strain curve (Schubnel et al., 2006). In this nonlinear regime, grain boundary geometry limits the propagation of intergranular microfractures, and intragranular microfractures propagated instead (Richter et al., 1976). The impact of grain boundaries on microfracture propagation is illustrated in our results by a lower cutoff in the power law distribution of increment sizes (Figure 10).

5.2. Interpreting Failure in Carrara Marble as a Critical Phase Transition

Our detailed tracking of microfracturing during compressive failure revealed that several observables such as the incremental damage, $dD_\varphi/d\Delta_D$, the largest microfracture, $S_{\max}$, or the distribution of fracture increment sizes evolve toward failure following specific scaling laws, up to at least $\Delta_D \approx 10^{-2}$. These scaling laws argue for an interpretation of compressive failure as a critical phase transition from an intact to a failed state (Alava et al., 2006; Girard et al., 2010; Vu et al., 2019). Different theoretical models can be proposed to interpret such critical transition, yielding specific scaling laws and critical exponents (Renard, Weiss, et al., 2018). A comparison of these predictions with our results is detailed below.

The simplest possible scenario would be a percolation of microfractures to form a system-spanning fault. It is known that the problem of failure of heterogeneous media can be mapped onto the percolation problem in case of infinite disorder (Roux et al., 1988). In that case, microfractures nucleate randomly and do not mechanically interact. If classical percolation predicts a power law divergence of the largest cluster, $S_{\max}$, as approaching the critical transition (the percolation threshold), the control parameter of this transition is the total damage itself, not the stress. In addition, percolation theory does not account for an evolution of the incremental damage or of the damage increments. Therefore, the compressive failure of Carrara marble cannot be mapped onto this theoretical framework.

This result points out to the crucial role of mechanical interactions between microfractures during the compressive failure process and suggests an analogy with another class of critical phenomena. Namely, the depinning transition (Ertaş & Kardar, 1994; Fisher, 1998) and the yielding transition (Lin et al., 2015; Nicolas et al., 2018) both share three fundamental ingredients with our problem: a local threshold mechanics, disorder, and elastic long-ranged interactions. In our experiments, the initial disorder in the rock arises from local strength heterogeneities related to pores, joints, and grain boundaries. The progressive clustering of microfracturing events toward sample failure results from long-ranged elastic interactions between cracks. Another prerequisite to observe such critical transition is a slow-driving condition. In our experiments, the loading (stress) rate was well below the rate of elastic stress relaxation after microfracturing events or the mean duration of avalanches of microfracturing events, both having time scales comparable to the propagation of elastic waves in the solid. Here, we compare the power law exponents obtained from the data with those predicted by theoretical frameworks or obtained by numerical models of damage in nonporous solids (Table 2) and discuss the quantitative deviations from predicted values.

Fisher et al. (1997) and Fisher (1998) have interpreted fault slip initiation as a depinning transition. These studies considered that during the initiation phase, the faults progressively unpin from the rock matrix before generalized frictional sliding takes place at the depinning transition. Brittle compressive failure of heterogeneous materials was also recently mapped to the depinning transition (Vu et al., 2019; Weiss et al., 2014), and associated predictions for system size effects on failure strength were proposed (Vu et al., 2018). The scaling predictions of the depinning framework are qualitatively consistent with our observations, in terms of incremental damage evolution, largest damage increment, or distribution of damage increments (see Table 2). The mean field description of the depinning transition provides predictions for the

Table 2
List of Scaling Exponents Calculated in Models of Compressive Failure in Heterogeneous Materials and Comparison With our Data on Carrara Marble

Scaling property (row) Models (column)	Incremental damage $dD_\varphi/d_{D\sim D}^{-\beta}$	Distribution of damage increment volumes at the critical point $P(s)\sim s^{-\alpha}$	Distribution of damage increment volumes (potency) at the critical point	Upper cut-off $s^{*}\sim^{-\gamma}$ (damage increment volume), or $P_0^{*}\sim^{-\gamma_P}$ (potency)	Correlation length $\xi\sim^{-\nu}$
Classical percolation (Stauffer, 1979)	No	No	No	No	$\nu \approx 0.8$ in 3-D
Depinning (mean field; LeBlanc et al., 2013; Weiss et al., 2014)	$\beta = \gamma(2-\alpha) = 1$	—	α=1.5	γ=2.0	$\nu = 1.0$
Yielding transition (Lin et al., 2015; Nicolas et al., 2018)	$\beta = \gamma(2-\alpha) \approx 1.1$	—	$\alpha_P \approx 1.5$ in 3-D	$\gamma_P \approx 2.3$ in 3-D	$\nu \approx 0.7$
Progressive damage model (Girard et al., 2010; Girard et al., 2012)	$\beta = \gamma(2-\alpha) \approx 0.4$	—	α=1.8 in 2-D	γ2.0 in 2-D	$\nu = 1.0 \pm 0.1$
The present study	$\beta = 2.6$	$\alpha = 2.1$	α=1.75	$\gamma = 2.5$ γ=3.6	$\nu = \frac{\gamma}{d_f} = 1.15$

critical exponents (LeBlanc et al., 2013), which were found to be in remarkable agreement with exponents obtained from an acoustic emission analysis of the compressive failure of concrete (Vu et al., 2019).

To compare our results with this theoretical framework, one must first clarify the definition of the size of a damage event. In the measurements detailed above, the size, s, of a damage increment is defined as the volume of the associated porosity. As this volume scales as $s\sim L^{d_f}$ with $d_f \approx 2.2$ (Figure 9), the so-defined "size" actually measures essentially the rupture area. In the interpretation of fault slip initiation (Fisher et al., 1997) or of compressive failure as a depinning transition (Vu et al., 2019), the damage avalanche size is defined instead as the integral of slip or displacement u over this rupture area A, that is, scales as a seismic potency, $P_0 = \int_A du$. Therefore, in order to link our measure of the size s of the damage increment with the avalanche size (or potency), a hypothesis has to be done about the average slip $\langle u \rangle$ over the rupture area. The classical assumption is $\langle u \rangle \sim L$ (Scholz & Cowie, 1990), which would give $P_0 \sim \langle u \rangle s \sim L^{3.2} \sim s^{1.45}$. Hence, the scaling $P(s)\sim s^{-\alpha} f(s/s^{*})$ with $s^{*}\sim\Delta^{-\gamma}$ (see section 4.3) can be translated into an avalanche size scaling $P(P_0)\sim P_0^{-\alpha_P} f\left(P_0/P_0^{*}\right)$, with $P_0^{*}\sim\Delta^{-\gamma_P}$, and the corresponding exponents given by $\alpha_P = \frac{\alpha+0.45}{1.45} \approx 1.75$ and $\gamma_P = 1.45\gamma \approx 3.6$. If the value of α_P compares relatively well with the mean field depinning exponent (1.5; see Table 2), γ_P is significantly larger than the depinning value (2.0). On the other hand, the correlation length exponent $\nu = 1.15$, whose estimation does not rely on an assumption about the average slip (see section 4.3), is in close agreement with the depinning prediction ($\nu = 1.0$).

However, when comparing the compressive failure of rocks with the depinning transition, one important point should be kept in mind regarding the nature of the elastic interaction kernel. In classical depinning, this kernel is assumed to be convex, meaning that stress (or force) redistribution after a depinning event occurs equally in all directions. This precludes a progressive localization of damage toward an incipient shear fault. This assumption represents a significant shortcoming to explain our observations. The yielding transition, describing the onset of plastic flow in amorphous media, integrates a nonconvex elastic interaction kernel, allowing strain localization along plastic shear bands (Lin et al., 2015; Nicolas et al., 2018). In terms of avalanches statistics, the yielding transition is similar to the depinning transition, with slightly different exponents (see Table 2). The agreement with our values is correct for α_P and ν but not for γ_P (see Table 2). As the yielding transition does not, in its classical formulation, incorporate friction (i.e., a role of pressure on microfracture nucleation or growth), the orientation of the macroscopic faults in our experiments, at 30° of the maximum principal stress, is not captured by this theoretical framework.

To circumvent the simplifying assumptions of these theoretical frameworks, progressive damage models have been developed (Amitrano et al., 1999; Tang, 1997). These models incorporate microstructural disorder from a distribution of local damage thresholds, internal friction in the form of a local Coulomb damage criterion, long-range elastic stress redistributions following damage events, and, more recently, a partition between elastic (small) and permanent (large) deformations, as well as healing mechanisms (Weiss &

Dansereau, 2017). They successfully capture the characteristics of brittle compressive failure for low-porosity rocks. Damage and strain localization arise naturally because the elastic kernel is nonconvex. The 2-D simulations have shown power law distributions of damage avalanche sizes with an upper cutoff becoming system spanning as approaching the maximum (failure) stress (Girard et al., 2010; Girard et al., 2012), which is analogous to microfracture increments distributions computed from our results. Similarly, the results of Figure 8 for the largest microfracture are qualitatively consistent with the growth of the largest damage cluster in this progressive damage model (Girard et al., 2012). Overall, the agreement between our results and the progressive damage model in terms of incremental damage, distributions of microfracture increments, or of the largest fracture/damage cluster, including in terms of exponents for α_P and ν (see Table 2), suggests an interpretation of the compressive failure of Carrara marble as a critical transition.

Concerning the scaling of the incremental damage, dD_φ/Δ_D (Figure 7a), it is worth stressing that the above-mentioned models do not predict an increasing damage event rate $dN/d\Delta_D$ when approaching the critical point. Therefore, our observations strongly differ from these models on this specific point but are in agreement with the acoustic emission monitoring of the compressive failure of nonporous heterogeneous materials (Vu et al., 2019). In our case, the incremental damage evolution results from both the evolution of the distribution of damage avalanche sizes and the evolution of the damage event rate. This might explain the difference between these modeling frameworks and our results in terms of exponent β; as in the case of the compressive failure of marble, the changing distribution combines with an increasing event rate. In addition, acoustic emissions measurements have shown that the p-exponent of the inverse Omori's scaling can vary with the material considered (e.g., Ojala et al., 2004; Vasseur et al., 2015). Hence, the variability of β, when compared with previous studies on quartz-monzonite (Renard, McBeck, et al., 2019; Renard, Weiss, et al., 2018), might come from the nature of the rock itself, through the variability on p.

Beyond this critical interpretation of compressive failure, we have shown on Figure 7 that the power law scaling of the incremental damage seems to break off very close to the failure stress ($\Delta_D < 0.02$), which is associated with a decreasing event rate. This is accompanied by few outliers in the tail of the distribution of increments (Figure 10). These observations indicate a possible departure from the critical scenario just before macroscopic faulting. The possible mechanisms associated with this breaking of scaling are discussed in the following.

5.3. Breaking of Scaling Near the Critical Point

Different mechanisms, or a combination of them, can be tentatively proposed to explain this breaking of scaling near the critical point. Note first that the two observations mentioned above might appear contradictory at first sight: whereas the near-failure dynamics is characterized by few, anomalously large damage increments (outliers on Figure 10), the global incremental damage itself does not accelerate as a power law in the vicinity of failure. We also stress that such breaking on the incremental damage scaling was not observed for quartz-monzonite (Renard, McBeck, et al., 2019; Renard, Weiss, et al., 2018), while damage increments were not analyzed in this material and less 3-D tomography data were acquired near failure.

The first possible mechanism is a subcritical growth of an incipient fault, corresponding to a slow (aseismic) crack growth under a stress intensity factor below the toughness of the material (Atkinson, 1982). In this case, one (or few) large damage cluster(s) could grow even during the constant stress conditions prevailing during the final 90-s stress steps needed to scan the sample (see section 3.1), whereas smaller clusters would remain unchanged. However, as mentioned in section 3.1, we did not detect a blurring of the radiographs, suggesting that fracture growth during scan acquisition is probably limited.

Another possibility would be a coalescence of some damage clusters to form the final fault by bridging of the gaps and taking place through anomalously large fracture increments. The signs of fracture coalescence in our experiment are the outliers in the distribution of increments (Figures 10 and 11). The breaking of scaling near failure, visible in Figures 6 and 7, appears more as a consequence of such coalescence. In a progressive damage model, similar outliers in the tail of the damage cluster sizes distributions were reported after the peak load, accompanying the coalescence of preexisting clusters into a major fault (Girard et al., 2012). This is consistent with our results, although such coalescence seems to be triggered slightly before peak stress in the present case. Girard et al. (2012) also mentioned that, once the largest cluster becomes system spanning, further damage and deformation accumulate along this fault, inhibiting additional damage

elsewhere. This is also consistent with the AE monitoring of fracturing of granite under multiaxial compression (Lockner et al., 1991). Such inhibition could explain the breaking of scaling of the incremental damage dD_{φ}/Δ_D (Figure 7). Whatever the mechanisms involved, the point at which the incremental damage deviates from a power law evolution could therefore represent a signal that a rock volume is approaching system-size failure. Additional observations on other rocks would be needed to confirm this observation.

5.4. Implications for Fault Mechanics

The scaling laws associated with progressive damage/microfracturing in our experiments shed light on the evolution of acoustic emissions prior to failure in laboratory experiments (Lockner et al., 1991; Vu et al., 2019) and possibly on foreshock activity before large earthquakes (Jaumé & Sykes, 1999). In the present discussion, we are aware of the huge scale gap between the laboratory experiments and natural faults. Several studies have attempted to export the concept of a critical point and precursory phenomena to predict large earthquakes (Main, 1996 and references therein). The stress released by earthquakes into the surrounding volume drives the system away from criticality. Conversely, progressive tectonic loading drives it toward a future critical state (Jaumé & Sykes, 1999), increasing the probability of the next large earthquake. The onset of slip along a 2-D heterogeneous fault in a 3-D elastic solid, that is, earthquake nucleation, has been interpreted as a critical depinning transition and mean field exponents derived (Fisher, 1998; Fisher et al., 1997). A two-phase diagram was proposed for the behavior of such fault: the Gutenberg-Richter phase characterized by a power law distribution of slip event sizes with an exponential cutoff and a runaway phase characterized by small events as well as quasiperiodic occurrence of system-size earthquakes (Dahmen et al., 1998). This might be reminiscent of our observations. The Gutenberg-Richter phase would be analogous to the prefailure, damage development phase in a rock, controlled by elastic long-range stress interactions and characterized by the emergence of power laws. The runaway phase would be equivalent to the system-size failure resulting from the formation of a percolating cluster leading to frictional sliding. Hence, the dynamics of precursory microfracturing activity before faulting observed in our experiments may be used to interpret a possible precursory activity before large earthquakes on geological faults. In this context, a breaking of power law scaling (see section 5.3), signing the transition from the Gutenberg-Richter phase to the runaway phase, could be the ultimate precursory signal before large earthquakes.

However, the possible prediction of large earthquakes on such basis remains an unsolved problem. If many large earthquakes seem to be preceded by foreshocks as well as a divergence of the seismic moment release rate (Jaumé & Sykes, 1999), these precursory phenomena are far to be ubiquitous (Bouchon et al., 2013; de Arcangelis et al., 2016; Zaliapin & Ben-Zion, 2013). Foreshocks could actually result from cascades of triggered seismicity implying that earthquakes are "predictable" to the same degree whatever their size (Helmstetter & Sornette, 2003). The use of these potential precursors as an earthquake forecasting tool remains therefore elusive so far. This raises important questions, such as the difference between the compressive failure of initially unfaulted rocks (this work) and the earthquake nucleation along a preexisting crustal fault, and calls for further theoretical and experimental work as well as geophysical data analysis.

6. Conclusions

We describe 3-D experimental data that reveal the spatial distribution of nucleating, propagating, and coalescing microfractures during the brittle compressive failure of Carrara marble rock samples. Our novel experimental setup allows in situ imaging of the sample during deformation and so enables the computation of statistical properties of the volume of microfractures and the derivation of scaling laws through which we quantify the critical nature of the failure process. We quantified the behavior of precursory microfracture events preceding macroscopic failure. The incremental damage showed power law acceleration with increasing stress up to ~98% of the failure stress and then transitioned to an exponential evolution in the vicinity of system-size failure. This evolution from power law to exponential appears therefore as the ultimate precursory signal of material failure.

Scaling laws pertaining to prepeak phase described the evolution of damage increments. The distribution of the sizes of microfracture increments showed power law scaling with exponential cutoff at large sizes. This cutoff itself is related to the correlation length of the damage process and increases toward failure, possibly through a power law divergence. The volume of the percolating largest fracture network diverged as well toward failure and could serve as an order parameter for failure interpreted as a critical phase transition

(Girard et al., 2012). Thus, brittle compressive failure in Carrara marble is a complex process that involves long-range elastic interactions, growth, nucleation, and coalescence of microfractures, leading to clustering, faulting, frictional sliding along faults, grain size reduction, and elastic softening. Scaling laws obtained from our data are in agreement with the damage models listed in Table 2. However, substantial differences in terms of the scaling exponents, their ranges, and a breaking of power law scaling very close to failure for the incremental damage are observed in our experimental data. Although the existence of power laws argues for a critical interpretation of failure (e.g., LeBlanc et al., 2013; Weiss et al., 2014; Girard et al., 2010; Girard et al., 2012), a complete micromechanical model that explains brittle failure under compression and that reproduces all these microstructural evolutions is still lacking. Breaking of scaling just before failure is understood as a complex interplay between microstructural phenomena such as subcritical crack growth and coalescence of large damage clusters.

Acknowledgments
The deformation apparatus was built by Sanchez Technology. Paul Tafforeau and Alexander Rack provided advice on the design of the tomography setup. This study received funding from the Norwegian Research Council (project HADES, Grant 250661). Beamtime was allocated at the European Synchrotron Radiation Facility (Long-Term Proposal ES-295). Data storage was provided by UNINETT Sigma2—the National Infrastructure for High Performance Computing and Data Storage in Norway (project NS9073K), and the experimental data can be obtained from the archive (https://doi.org/10.11582/2019.00001). The dynamic 3-D microtomography of the two Carrara marble samples is available freely through the UNINETT Sigma2 repository (https://doi.org/10.11582/2019.00001). The authors thank Jess McBeck for a careful review of an early draft of this manuscript.

References

Alava, M. J., Nukala, P. K., & Zapperi, S. (2006). Statistical models of fracture. *Advances in Physics*, *55*(3–4), 349–476. https://doi.org/10.1080/00018730300741518

Amitrano, D., Grasso, J. R., & Hantz, D. (1999). From diffuse to localised damage through elastic interaction. *Geophysical Research Letters*, *26*(14), 2109–2112. https://doi.org/10.1029/1999GL900388

Atkinson, B. K. (1982). Subcritical crack propagation in rocks: Theory, experimental results and applications. *Journal of Structural Geology*, *4*(1), 41–56. https://doi.org/10.1016/0191-8141(82)90005-0

Bell, A. F., Naylor, M., & Main, I. G. (2013). The limits of predictability of volcanic eruptions from accelerating rates of earthquakes. *Geophysical Journal International*, *194*(3), 1541–1553. https://doi.org/10.1093/gji/ggt191

Bouchon, M., Durand, V., Marsan, D., Karabulut, H., & Schmittbuhl, J. (2013). The long precursory phase of most large interplate earthquakes. *Nature Geoscience*, *6*(4), 299–302. https://doi.org/10.1038/ngeo1770

Bouchon, M., Karabulut, H., Aktar, M., Özalaybey, S., Schmittbuhl, J., & Bouin, M. P. (2011). Extended nucleation of the 1999 Mw 7.6 Izmit earthquake. *Science*, *331*(6019), 877–880. https://doi.org/10.1126/science.1197341

Brace, W. F., & Bombolakis, E. G. (1963). A note on brittle crack growth in compression. *Journal of Geophysical Research*, *68*(12), 3709–3713. https://doi.org/10.1029/JZ068i012p03709

Brace, W. F., Paulding, B. W. Jr., & Scholz, C. H. (1966). Dilatancy in the fracture of crystalline rocks. *Journal of Geophysical Research*, *71*(16), 3939–3953. https://doi.org/10.1029/JZ071i016p03939

Brace, W. F., Silver, E., Hadley, K., & Goetze, C. (1972). Cracks and pores: A closer look. *Science*, *178*(4057), 162–164. https://doi.org/10.1126/science.178.4057.162

Buades, A., Coll, B., & Morel, J. M. (2005). A review of image denoising algorithms, with a new one. *Multiscale Modeling & Simulation*, *4*(2), 490–530.

Clauset, A., Shalizi, C. R., & Newman, M. E. (2009). Power-law distributions in empirical data. *SIAM Review*, *51*(4), 661–703. https://doi.org/10.1137/070710111

Dahmen, K., Ertaş, D., & Ben-Zion, Y. (1998). Gutenberg-Richter and characteristic earthquake behavior in simple mean-field models of heterogeneous faults. *Physical Review E*, *58*(2), 1494–1501. https://doi.org/10.1103/PhysRevE.58.1494

Dahmen, K. A., Ben-Zion, Y., & Uhl, J. T. (2009). Micromechanical model for deformation in solids with universal predictions for stress-strain curves and slip avalanches. *Physical Review Letters*, *102*(17), 175501. https://doi.org/10.1103/PhysRevLett.102.175501

de Arcangelis, L., Godano, C., Grasso, J. R., & Lippiello, E. (2016). Statistical physics approach to earthquake occurrence and forecasting. *Physics Reports*, *628*, 1–91. https://doi.org/10.1016/j.physrep.2016.03.002

Ertaş, D., & Kardar, M. (1994). Critical dynamics of contact line depinning. *Physical Review E*, *49*(4), R2532–R2535. https://doi.org/10.1103/PhysRevE.49.R2532

Fisher, D. S. (1998). Collective transport in random media: From superconductors to earthquakes. *Physics Reports*, *301*(1–3), 113–150. https://doi.org/10.1016/S0370-1573(98)00008-8

Fisher, D. S., Dahmen, K., Ramanathan, S., & Ben-Zion, Y. (1997). Statistics of earthquakes in simple models of heterogeneous faults. *Physical Review Letters*, *78*(25), 4885–4888. https://doi.org/10.1103/PhysRevLett.78.4885

Fredrich, J. T., Evans, B., & Wong, T. F. (1989). Micromechanics of the brittle to plastic transition in Carrara marble. *Journal of Geophysical Research*, *94*(B4), 4129–4145. https://doi.org/10.1029/JB094iB04p04129

Fredrich, J. T., Menendez, B., & Wong, T. F. (1995). Imaging the pore structure of geomaterials. *Science*, *268*(5208), 276–279. https://doi.org/10.1126/science.268.5208.276

Girard, L., Amitrano, D., & Weiss, J. (2010). Failure as a critical phenomenon in a progressive damage model. *Journal of Statistical Mechanics: Theory and Experiment*, *2010*(01), P01013. https://doi.org/10.1088/1742-5468/2010/p01013

Girard, L., Weiss, J., & Amitrano, D. (2012). Damage-cluster distributions and size effect on strength in compressive failure. *Physical Review Letters*, *108*(22), 225502. https://doi.org/10.1103/PhysRevLett.108.225502

Griffith, A. A. (1921). VI. The phenomena of rupture and flow in solids. *Philosophical Transactions of the Royal Society of London Series A*, *221*(582–593), 163–198. https://doi.org/10.1098/rsta.1921.0006

Helmstetter, A., & Sornette, D. (2003). Foreshocks explained by cascades of triggered seismicity. *Journal of Geophysical Research*, *108*(B10), 2457. https://doi.org/10.1029/2003JB002409

Hoek, E., & Bieniawski, Z. T. (1965). Brittle fracture propagation in rock under compression. *International Journal of Fracture Mechanics*, *1*(3), 137–155.

Hoek, E., & Martin, C. D. (2014). Fracture initiation and propagation in intact rock—A review. *Journal of Rock Mechanics and Geotechnical Engineering*, *6*(4), 287–300. https://doi.org/10.1016/j.jrmge.2014.06.001

Iglauer, S., & Lebedev, M. (2017). High pressure-elevated temperature x-ray micro-computed tomography for subsurface applications. *Advances in Colloid and Interface Science*, *256*, 393–410.

Jaeger, J. C., & Cook, N. G. (1969). *Fundamentals of Rock Mechanics* (Vol. 513). London: Methuen & Co. Ltd.

Jaumé, S. C., & Sykes, L. R. (1999). Evolving towards a critical point: A review of accelerating seismic moment/energy release prior to large and great earthquakes. In *Seismicity patterns, their statistical significance and physical meaning* (pp. 279–305). Basel: Birkhäuser. https://doi.org/10.1007/978-3-0348-8677-2_5

Jha, D., Sørensen, H. O., Dobberschütz, S., Feidenhans'l, R., & Stipp, S. L. S. (2014). Adaptive center determination for effective suppression of ring artifacts in tomography images. *Applied Physics Letters*, *105*(14), 143107. https://doi.org/10.1063/1.4897441

Kato, A., Obara, K., Igarashi, T., Tsuruoka, H., Nakagawa, S., & Hirata, N. (2012). Propagation of slow slip leading up to the 2011 Mw 9.0 Tohoku-Oki earthquake. *Science*, *335*, 705–708. https://doi.org/10.1126/science.1215141

Kranz, R. L. (1983). Microcracks in rocks: A review. *Tectonophysics*, *100*(1–3), 449–480. https://doi.org/10.1016/0040-1951(83)90198-1

Kuksenko, V., Tomilin, N., Damaskinskaya, E., & Lockner, D. (1996). A two-stage model of fracture of rocks. *Pure and Applied Geophysics*, *146*(2), 253–263. https://doi.org/10.1007/BF00876492

LeBlanc, M., Angheluta, L., Dahmen, K., & Goldenfeld, N. (2013). Universal fluctuations and extreme statistics of avalanches near the depinning transition. *Physical Review E*, *87*(2), 022126. https://doi.org/10.1103/PhysRevE.87.022126

Lin, J., Gueudré, T., Rosso, A., & Wyart, M. (2015). Criticality in the approach to failure in amorphous solids. *Physical Review Letters*, *115*(16), 168001. https://doi.org/10.1103/PhysRevLett.115.168001

Lockner, D., Byerlee, J. D., Kuksenko, V., Ponomarev, A., & Sidorin, A. (1991). Quasi-static fault growth and shear fracture energy in granite. *Nature*, *350*(6313), 39–42. https://doi.org/10.1038/350039a0

Lockner, D. A., Byerlee, J. D., Kuksenko, V., Ponomarev, A., & Sidorin, A. (1992). Observations of quasistatic fault growth from acoustic emissions. *International Geophysics*, *51*, 3–31. https://doi.org/10.1016/S0074-6142(08)62813-2

Main, I. (1996). Statistical physics, seismogenesis, and seismic hazard. *Reviews of Geophysics*, *34*(4), 433–462. https://doi.org/10.1029/96RG02808

Malaga-Starzec, K., Lindqvist, J. E., & Schouenborg, B. (2002). Experimental study on the variation in porosity of marble as a function of temperature. *Geological Society, London, Special Publications*, *205*(1), 81–88. https://doi.org/10.1144/GSL.SP.2002.205.01.07

Mirone, A., Brun, E., Gouillart, E., Tafforeau, P., & Kieffer, J. (2014). The PyHST2 hybrid distributed code for high speed tomographic reconstruction with iterative reconstruction and a priori knowledge capabilities. *Nuclear Instruments and Methods in Physics Research Section B: Beam Interactions with Materials and Atoms*, *324*, 41–48. https://doi.org/10.1016/j.nimb.2013.09.030

Moore, D. E., & Lockner, D. A. (1995). The role of microcracking in shear-fracture propagation in granite. *Journal of Structural Geology*, *17*(1), 95–114. https://doi.org/10.1016/0191-8141(94)E0018-T

Nicolas, A., Ferrero, E. E., Martens, K., & Barrat, J. L. (2018). Deformation and flow of amorphous solids: Insights from elastoplastic models. *Reviews of Modern Physics*, *90*(4), 045006. https://doi.org/10.1103/RevModPhys.90.045006

Ojala, I. O., Main, I. G., & Ngwenya, B. T. (2004). Strain rate and temperature dependence of Omori law scaling constants of AE data: Implications for earthquake foreshock-aftershock sequences, *Geophysical Research Letters*, *31*, L24617. https://doi.org/10.1029/2004GL020781

Oesterling, N., Heilbronner, R., Stünitz, H., Barnhoorn, A., & Molli, G. (2007). Strain dependent variation of microstructure and texture in naturally deformed Carrara marble. *Journal of Structural Geology*, *29*(4), 681–696. https://doi.org/10.1016/j.jsg.2006.10.007

Ohnaka, M. (1992). Earthquake source nucleation: A physical model for short-term precursors. *Tectonophysics*, *211*(1–4), 149–178. https://doi.org/10.1016/0040-1951(92)90057-D

Paganin, D., Gureyev, T. E., Pavlov, K. M., Lewis, R. A., & Kitchen, M. (2004). Phase retrieval using coherent imaging systems with linear transfer functions. *Optics Communications*, *234*(1-6), 87–105. https://doi.org/10.1016/j.optcom.2004.02.015

Paterson, M. S., & Wong, T. F. (2005). *Experimental rock deformation-the brittle field*. Heidelberg: Springer Science & Business Media.

Peng, S., & Johnson, A. M. (1972). Crack growth and faulting in cylindrical specimens of Chelmsford granite. *International Journal of Rock Mechanics and Mining Sciences & Geomechanics Abstracts*, *9*(1), 37–86). Pergamon. https://doi.org/10.1016/0148-9062(72)90050-2

Renard, F., Cordonnier, B., Dysthe, D. K., Boller, E., Tafforeau, P., & Rack, A. (2016). A deformation rig for synchrotron microtomography studies of geomaterials under conditions down to 10 km depth in the earth. *Journal of Synchrotron Radiation*, *23*(4), 1030–1034. https://doi.org/10.1107/S1600577516008730

Renard, F., Cordonnier, B., Kobchenko, M., Kandula, N., Weiss, J., & Zhu, W. (2017). Microscale characterization of rupture nucleation unravels precursors to faulting in rocks. *Earth and Planetary Science Letters*, *476*, 69–78. https://doi.org/10.1016/j.epsl.2017.08.002

Renard, F., McBeck, J., Cordonnier, B., Zheng, X., Kandula, N., Sanchez, J. R., et al. (2019). Dynamic in situ three-dimensional imaging and digital volume correlation analysis quantify strain localization and fracture coalescence in sandstone. *Pure and Applied Geophysics*, *176*(3), 1083–1115. https://doi.org/10.1007/s00024-018-2003-x

Renard, F., Weiss, J., Mathiesen, J., Ben-Zion, Y., Kandula, N., & Cordonnier, B. (2018). Critical evolution of damage toward system-size failure in crystalline rock. *Journal of Geophysical Research: Solid Earth*, *123*(2), 1969–1986. https://doi.org/10.1002/2017JB014964

Richter, D., Simmons, G., & Siegfried, R. (1976). Microcracks, micropores, and their petrologic interpretation for 72415 and 15418. In *Lunar and Planetary Science Conference Proceedings* (Vol. 7, pp. 1901–1923). New York: Pergamon Press.

Roux, S., Hansen, A., Herrmann, H., & Guyon, E. (1988). Rupture of heterogeneous media in the limit of infinite disorder. *Journal of Statistical Physics*, *52*(1–2), 237–244. https://doi.org/10.1007/BF01016411

Rutter, E. H. (1972). The influence of interstitial water on the rheological behaviour of calcite rocks. *Tectonophysics*, *14*(1), 13–33. https://doi.org/10.1016/0040-1951(72)90003-0

Scholz, C. H., & Cowie, P. A. (1990). Determination of total strain from faulting using slip measurements. *Nature*, *346*(6287), 837.

Schubnel, A., Walker, E., Thompson, B. D., Fortin, J., Guéguen, Y., & Young, R. P. (2006). Transient creep, aseismic damage and slow failure in Carrara marble deformed across the brittle-ductile transition. *Geophysical Research Letters*, *33*, L17301. https://doi.org/10.1029/2006GL026619

Sornette, D. (1994). Sweeping of an instability: An alternative to self-organized criticality to get power laws without parameter tuning. *Journal de Physique I*, *4*(2), 209–221. https://doi.org/10.1051/jp1:1994133

Stanley, H. E. (1999). Scaling, universality, and renormalization: Three pillars of modern critical phenomena. *Reviews of Modern Physics*, *71*(2), S358. https://doi.org/10.1103/RevModPhys.71.S358

Stauffer, D. (1979). Scaling theory of percolation clusters. *Physics Reports*, *54*(1), 1–74. https://doi.org/10.1016/0370-1573(79)90060-7

Sternberg, S. (1983). Biomedical image processing. *Computer*, *16*(1), 22–34. https://doi.org/10.1109/MC.1983.1654163

Tal, Y., Evans, B., & Mok, U. (2016). Direct observations of damage during unconfined brittle failure of Carrara marble. *Journal of Geophysical Research: Solid Earth*, *121*, 1584–1609. https://doi.org/10.1002/2015JB012749

Tang, C. A. (1997). Numerical simulation of progressive rock failure and associated seismicity. *International Journal of Rock Mechanics and Mining Sciences*, *34*(2), 249–261. https://doi.org/10.1016/S0148-9062(96)00039-3

Tapponnier, P., & Brace, W. F. (1976). Development of stress-induced microcracks in westerly granite. *International Journal of Rock Mechanics and Mining Science & Geomechanical Abstracts*, *13*(4), 103–112. https://doi.org/10.1016/0148-9062(76)91937-9

Vasseur, J., Wadsworth, F. B., Lavallée, Y., Bell, A. F., Main, I. G., & Dingwell, D. B. (2015). Heterogeneity: the key to failure forecasting. *Scientific Reports*, *5*, 13259.

Vu, C. C., Amitrano, D., Plé, O., & Weiss, J. (2019). Compressive failure as a critical transition: Experimental evidence and mapping onto the universality class of depinning. *Physical Review Letters*, *122*(1), 015502. https://doi.org/10.1103/PhysRevLett.122.015502

Vu, C. C., Weiss, J., Plé, O., Amitrano, D., & Vandembroucq, D. (2018). Revisiting statistical size effects on compressive failure of heterogeneous materials, with a special focus on concrete. *Journal of the Mechanics and Physics of Solids*, *121*, 47–70. https://doi.org/10.1016/j.jmps.2018.07.022

Wawersik, W. R., & Fairhurst, C. (1970). A study of brittle rock fracture in laboratory compression experiments. *International Journal of Rock Mechanics and Mining Sciences & Geomechanics Abstracts*, *7*(5), 561–575). Pergamon. https://doi.org/10.1016/0148-9062(70)90007-0

Weiss, J., & Dansereau, V. (2017). Linking scales in sea ice mechanics. *Philosophical Transactions of the Royal Society A*, *375*(2086), 20150352. https://doi.org/10.1098/rsta.2015.0352

Weiss, J., Girard, L., Gimbert, F., Amitrano, D., & Vandembroucq, D. (2014). (Finite) statistical size effects on compressive strength. *Proceedings of the National Academy of Sciences*, *111*(17), 6231–6236. https://doi.org/10.1073/pnas.1403500111

Wong, L. N. Y., & Einstein, H. H. (2009). Crack coalescence in molded gypsum and Carrara marble: Part 1. Macroscopic observations and interpretation. *Rock Mechanics and Rock Engineering*, *42*(3), 475–511. https://doi.org/10.1007/s00603-008-0002-4

Wong, T. F., Wong, R. H., Chau, K. T., & Tang, C. A. (2006). Microfracture statistics, Weibull distribution and micromechanical modeling of compressive failure in rock. *Mechanics of Materials*, *38*(7), 664–681. https://doi.org/10.1016/j.mechmat.2005.12.002

Wu, C., Meng, X., Peng, Z., & Ben-Zion, Y. (2013). Lack of spatiotemporal localization of foreshocks before the 1999 M w 7.1 Düzce, Turkey, earthquake. *Bulletin of the Seismological Society of America*, *104*(1), 560–566. https://doi.org/10.1785/0120130140

Zaliapin, I., & Ben-Zion, Y. (2013). Earthquake clusters in southern California I: Identification and stability. *Journal of Geophysical Research: Solid Earth*, *118*, 2847–2864. https://doi.org/10.1002/jgrb.50179